Geosciences and Engineering, Vol. 13, No. 1 (2025), pp. 45–58.
https://doi.org/10.33030/geosciences.2025.01.004

MECHANOCHEMICALLY SYNTHESIZED TERNARY CHALCOGENIDE $CuInSe_2/TiO_2$ NANOCOMPOSITE FOR SOLAR CELL APPLICATIONS

ERIKA DUTKOVÁ[1, *], MATEJ BALÁŽ[2], JAROSLAV KOVÁČ[3], ADELIA KASHIMBETOVA[4], JAROSLAV BRIANČIN[5], JAROSLAV KOVÁČ, Jr.[6], LADISLAV ČELKO[7]

[1, *]*Institute of Geotechnics Slovak Academy of Sciences, Slovakia; dutkova@saske.sk*
[2]*Institute of Geotechnics Slovak Academy of Sciences, Slovakia; balazm@saske.sk*
[3]*Institute of Electronics and Photonics, Slovak University of Technology, Slovakia; jaroslav.kovac@stuba.sk*
[4]*Central European Institute of Technology, Brno University of Technology, Czech Republic; kashimbetova@vutbr.cz*
[5]*Institute of Geotechnics Slovak Academy of Sciences, Slovakia; briancin@saske.sk*
[6]*Institute of Electronics and Photonics, Slovak University of Technology, Slovakia; jaroslav_kovac@stuba.sk*
[7]*Central European Institute of Technology, Brno University of Technology, Czech Republic; ladislav.celko@ceitec.vutbr.cz*

Abstract: In this paper, the simple mechanochemical synthesis of $CuInSe_2/TiO_2$ nanocomposite is described. $CuInSe_2/TiO_2$ nanocomposite was characterized from the crystal structure, microstructural, morphology, surface, optical, and optoelectrical properties viewpoints. X-ray diffraction has confirmed the nanocrystalline character of all components of the nanocomposite, the crystallite size for $CuInSe_2$ (18 nm) being larger than in the case of both TiO_2 phases (5 and 8 nm for rutile and anatase, respectively). Raman spectroscopy confirmed the presence of both components in the synthesized nanocomposite. SEM has shown that the nanoparticles are agglomerated into larger grains. High-resolution XPS analysis confirmed the presence of all elements with their expected oxidation states. The measured optical properties using UV-Vis spectroscopy exhibit stronger absorption from the ultraviolet to visible region with the determined optical bandgap 1.3 eV for mechanochemically synthesized $CuInSe_2/TiO_2$ nanocomposite. The photocurrent increased by 57% in $CuInSe_2/TiO_2$ nanocomposite compared to $CuInSe_2$ under illumination in comparison with that in the dark state.

Keywords*: mechanochemistry, $CuInSe_2/TiO_2$, nanocomposite, optical properties, optoelectrical properties*

1. INTRODUCTION

Ternary chalcogenide semiconductors of I–III–VI group with promising applications in electronics, optics, and catalysis have been intensively studied in recent years (Klenk et al., 2011). However, the majority of the best investigated sulphide-based semiconductors contain toxic heavy metals, which seriously limit their potential application.

$CuInSe_2$ is also one of the promising semiconductive ternary materials applicable in high-efficiency solar cells and photocatalysis due to its large absorption coefficient, suitably small bandgap, large conversion efficiency and radiation stability (Guo et al., 2008; Kang et al., 2009). It is beneficial to couple $CuInSe_2$, a small bandgap semiconductor (its bulk bandgap is 1.05 eV) with the material with a larger bandgap, like TiO_2 (its bulk bandgap is 3.2 eV). Coupling these two components can improve optical properties due to the elimination of surface non-radiative recombination defects. $CuInSe_2/TiO_2$ nanocomposite can be an excellent alternative for solar cell applications (Yu et al., 2011; Das et al., 2017), as well as for the photocatalytic degradation of dyes in the visible light region.

There are several synthetic procedures for the preparation of $CuInSe_2/TiO_2$ nanomaterial, including thermal and microwave assisted hybridization (Kshirsagar et al., 2017), oxidative chemical polymerization method (Yu et al., 2011), electrodeposition technique (Valdes et al., 2011; Das et al., 2017), colloidal synthesis (Wu et al., 2015), electrophoretic deposition technique (Liao et al., 2013), simple successive ionic layer adsorption and reaction (SILAR) method (Wang et al., 2015), spin coating method (Zhang et al., 2020), electrochemical anodic oxidation and solvothermal synthesis (Yang et al., 2022).

Mechanochemistry as an environmentally friendly alternative to the traditional preparation methods is well-applicable in the field of materials science. The high-energy milling process is used either as a synthesis step to prepare inorganic nanomaterials applicable in advanced applications or to introduce defects into the crystalline structure, which can dramatically improve the application potential (Baláž et al., 2017).

To the best of our knowledge, the $CuInSe_2/TiO_2$ nanocomposite has not been prepared by mechanochemical synthesis so far. The novelty of this work is the simple and environmentally friendly mechanochemical method of $CuInSe_2/TiO_2$ nanocomposite preparation for a very short time, at ambient pressure and temperature as a suitable material for solar cell applications.

2. MATERIALS AND METHODS

2.1. Materials

For the synthesis of $CuInSe_2/TiO_2$ nanocomposite were used: elemental copper (99.7%, Merck, Darmstadt, Germany), indium (99.99%, Aldrich, Taufkirchen, Germany), selenium (99.5% Aldrich, Taufkirchen, Germany) and commercially available TiO_2 Degussa P25 (Degussa, Netherland) (75% anatase and 25% rutile).

2.2. Methods

$CuInSe_2/TiO_2$ nanocomposite was synthesized by a two-step process. In the first step (Equation 1), $CuInSe_2$ was prepared by milling 0.94 g of copper, 1.71 g of indium and 2.35 g of selenium. The milling was carried out in a planetary mill Pulverisette 6 (Fritsch, Idar-Oberstein, Germany) at 550 rpm using a tungsten carbide milling

chamber (250 mL in volume) and 50 balls (360 g) with 10 mm in diameter, composed of the same material, during 60 min in an argon atmosphere according the procedure described in (Dutkova et al., 2016). The ball-to-powder ratio was 72:1. In the second step, 2.5 g of TiO_2 was introduced into milling with 2.5 g of previously synthesized $CuInSe_2$. Co-milling (Equation 2) was also performed in a planetary mill Pulverisette 6 (Fritsch, Idar-Oberstein, Germany) in an argon atmosphere (>99.998%, Linde Gas group, Bratislava, Slovakia) for 30 min without break cooling due to shorter milling times. The milling chamber was vented with Ar gas for 3 min providing an inert atmosphere. The 250 mL tungsten carbide milling chamber with 50 tungsten carbide balls with 10 mm in diameter was used. The rotational speed of the planet carrier was 500 rpm. The ball-to-powder ratio was 72:1.

The synthesis of $CuInSe_2/TiO_2$ nanocomposite can be described by the following Equations 1–2:

$$Cu + In + 2Se \rightarrow CuInSe_2 \quad (1)$$

$$CuInSe_2 + TiO_2 \rightarrow CuInSe_2/TiO_2 \quad (2)$$

2.3. Characterization techniques

X-ray diffraction (XRD) measurements were performed using a D8 Advance diffractometer (Bruker, Bremen, Germany) equipped with a θ-θ goniometer, CuK_α radiation (40 kV, 40 mA), a secondary graphite monochromator, and a scintillation detector. All samples were scanned from 15° to 70° with the step 0.03° and 12 s counting time. Diffracplus Eva software was used for phase analysis according to the ICDD - PDF2 database. The Rietveld refinement was performed using a TOPAS Academic software (Evans, 2010; Coelho, 2018).

The micro-Raman and micro-PL measurements were performed in air at room temperature, with the focus of the beam of an Ar laser (514 nm) via a confocal Raman Microscope (Spectroscopy & Imaging, Warstein, Germany) in backscattering geometry. The frequency of the Raman line of crystalline Si at 520 cm^{-1} was used to calibrate the system in the present study.

Morphology was investigated using a field emission-scanning electron microscope (FE-SEM, Mira 3, Tescan, Czech Republic) coupled with an EDX analyzer (Oxford Instruments).

The values of the specific surface area were received by using a NOVA 1200e Surface Area & Pore Size Analyzer (Quantachrome Instruments, Boynton Beach, FL, USA).

The X-ray photoelectron spectroscopy (XPS) measurements were performed in the XPS Kratos Axis Supra apparatus (Manchester, UK) with a monochromatic AlKα X-ray radiation, an emission current of 15 mA, and a hybrid lens model. XPS survey and high-resolution (HR) spectra were recorded using scanning steps of 1.0 and 0.1 eV, respectively. The obtained data were calibrated by setting the C1s emission at 284.8 eV. The deconvolution and fitting of the interesting elements were carried out using the CasaXPS software (version 2.3.17) by applying a Spine Shirley

background in the high-resolution spectra and a Gaussian/Lorentzian line shape for fitting the XPS peaks.

Absorption spectra were recorded using a UV-Vis spectrophotometer Helios Gamma (Thermo Electron Corporation, Warwickshire, UK) in a quartz cell by dispersing the synthesized particles in absolute ethanol by ultrasonic stirring. The band gap energy (Eg) was determined by utilization of Tauc equation (3):

$$(\alpha h\nu)^{1/n} = A(h\nu - E_g) \tag{3}$$

where α is the absorption coefficient, A is a constant, h = Planck's constant, ν = frequency and n is a constant associated with different kinds of electronic transitions (0.5 for a direct allowed, 2 for an indirect allowed, 1.5 for a direct forbidden and 3 for an indirect forbidden). The optical band gap, Eg was estimated by plotting $(\alpha h\nu)^2$ as a function of the photon energy hν. Extrapolating the straight line portion of the Tauc plot for zero absorption coefficient (α = 0) gives optical bandgap energy.

The current-voltage (I-V) characteristics were measured using semiconductor parameter analyzer Agilent 4155C under dark and focused halogen white light illumination (illumination intensity of ~ 600 mW/cm^2). The measured sample was separated from crushing pellets to small pieces (thin stripe with dimensions ~ 200-500 μm) and transferred onto insulating pad. The sample contacts were made by small droplet of silver paste and then annealed together with wiring to the socket.

3. Results and Discussion

3.1. Structural characterization

The X-ray diffraction (XRD) patterns of previously mechanochemically prepared $CuInSe_2$, commercial TiO_2 and mechanochemically synthesized $CuInSe_2/TiO_2$ nanocomposite are shown in Fig. 1. The Rietveld refinement was carried out to study the phase composition and crystallite size of the produced nanocomposite (Figure 2). The diffractions of both components of the nanocomposite can be well-seen in the figure. Surprisingly, the reflections corresponding to tetragonal $CuInSe_2$, the content of which is same with content of TiO_2, are more intensive that of TiO_2. This means that the crystallite size of selenide seems to be larger than in the case of titanium dioxide. With regards to TiO_2, commercial Degussa P25 with the 75% content of anatase and 25% of rutile has been used. However, the reflections corresponding to the latter are more pronounced, so it seems that the anatase-to-rutile phase transformation took place during milling, which has been previously observed (Kostova and Dutkova, 2016). According to Rietveld refinement, the estimated crystallite size of $CuInSe_2$ is 18 ±5 nm and the detected microstrain is 2.1 ±0.4%. $CuInSe_2$ crystallized in I-42d space group with the following refined lattice parameters a = 5.753 ±0.014 Å and c = 11.595 ±0.017 Å. For titanium dioxide phases, the estimated crystallite size is 5 ±1 and 8 ±1 nm for rutile and anatase, respectively, which confirms the presence of very fine crystallites and broad diffractions with low intensity detected for TiO_2 in the XRD pattern. TiO_2-anatase crystallized in I41/amd space group with the refined lattice parameters a = 3.764 ±0.007 Å

and c = 9.47 ±0.023 Å. Another one TiO_2- rutile phase crystallized in P42/mnm space group with the refined lattice parameters a = 4.590 ±0.017 Å and c = 2.973 ±0.013 Å.

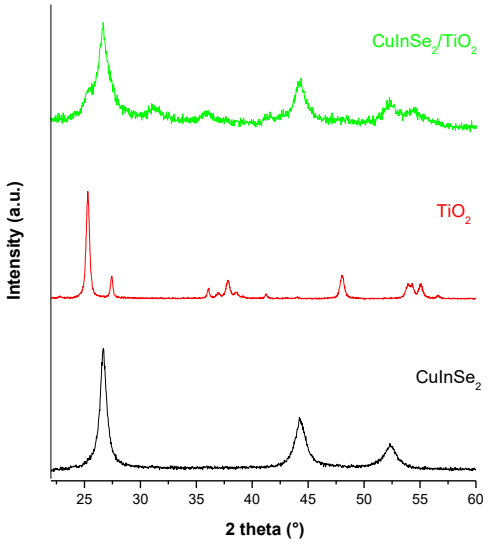

Figure 1
XRD patterns of $CuInSe_2$, TiO_2, and $CuInSe_2/TiO_2$ nanocomposite

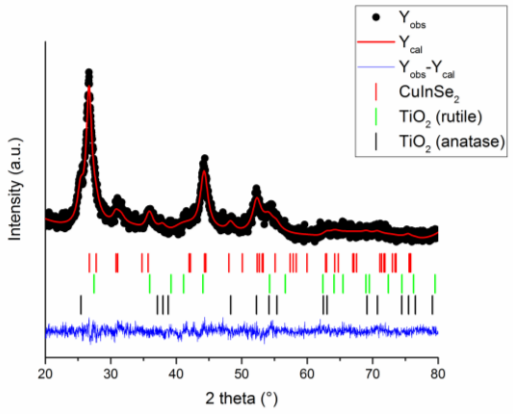

Figure 2
XRD pattern and the results of Rietveld refinement of $CuInSe_2/TiO_2$ nanocomposite

The micro-Raman spectra of the synthesized $CuInSe_2$, $CuInSe_2/TiO_2$ nanocomposite and commercially available TiO_2 under laser excitation at 514 nm are shown in Figure 3. The results of Raman spectrum of synthesized $CuInSe_2$ are in good agreement with previously published $CuInSe_2$ measurements (Rincon and Ramirez, 1992; Zaretskaya et al., 2003). The $CuInSe_2/TiO_2$ nanocomposite is a mixture of both components which are broadened upon interaction. The measured spectrum shows that

the dominant feature of Raman spectrum of $CuInSe_2/TiO_2$ nanocomposite are the peaks of TiO_2 showing the formation of a compound in various crystallographic forms – polymorphism (Tuschel, 2019). The intense peak at 146 cm^{-1} and a broad less intense peak at 250 cm^{-1} and near 395–440 cm^{-1} correspond to anatase form TiO_2 with symmetries E_g and B_{1g} and rutile form with symmetry E_g and E (Tuschel, 2019). The deflection near 173 cm^{-1} and peak at 208 cm^{-1} can be assigned to $CuInSe_2$ phase with symmetries A_1 and E. Raman spectroscopy confirmed the crystalline nanoparticles formation being in a good agreement with the results measured by XRD.

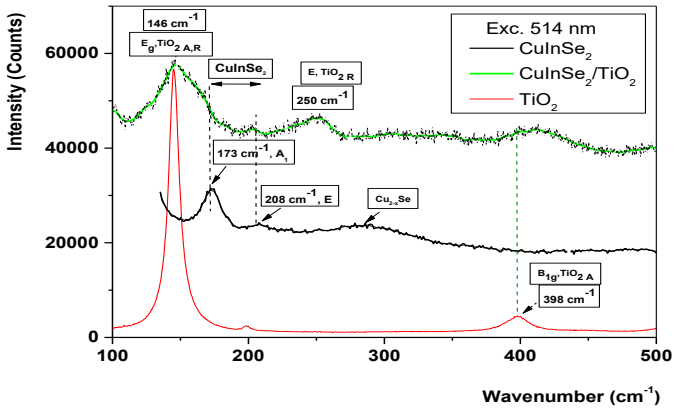

Figure 3

Micro-Raman spectrum of $CuInSe_2$, TiO_2, and $CuInSe_2/TiO_2$ nanocomposite

3.2. Surface and morphological characterization

The specific surface area (S_A) values belong to some of the most important characteristics of milled samples (Baláž et al., 2013). The S_A of pure $CuInSe_2$, from which the studied nanocomposite was prepared, is 2.9 m^2g^{-1} as was reported in (Dutkova et al., 2016). In the present study, the co-milling with TiO_2 led to a considerable increase of the specific surface area of the sample $CuInSe_2/TiO_2$ (13 m^2g^{-1}) in comparison with CuInSe2 alone. However, the obtained value is significantly lower than that acquired after the introduction of ZnS to $CuInSe_2$ reported in (Dutkova et al., 2021). Further, the S_A value of ZnS (108 m^2g^{-1}) is much higher than that of pure TiO_2 P25 (28.7 m^2g^{-1}). The achieved value of S_A for $CuInSe_2/TiO_2$ is far lower than in the other reports on similar systems applying different synthetic approaches (Kshirsagar et al., 2017).

The morphology of synthesized nanocomposite was studied by the means of scanning electron microscopy (SEM). SEM micrograph of the prepared $CuInSe_2/TiO_2$ nanocomposite is shown in Figure 4a. SEM image displays polydispersed particles, where the agglomerates exhibit the size in micrometers, however, smaller units with the sizes in the nanometer range can be clearly distinguished. The results of a representative EDX analysis are presented in Figure 4b. Several EDX analyses performed at different parts of the sample revealed a relatively homogeneous distribution of the elements present in $CuInSe_2/TiO_2$ nanocomposite.

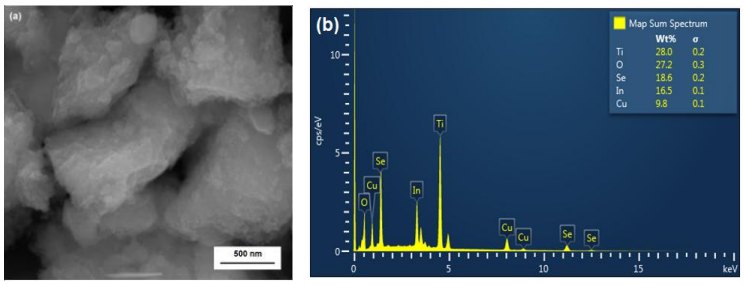

Figure 4

a) SEM image and (b) EDX spectrum recorded in characteristic parts of $CuInSe_2/TiO_2$ nanocomposite

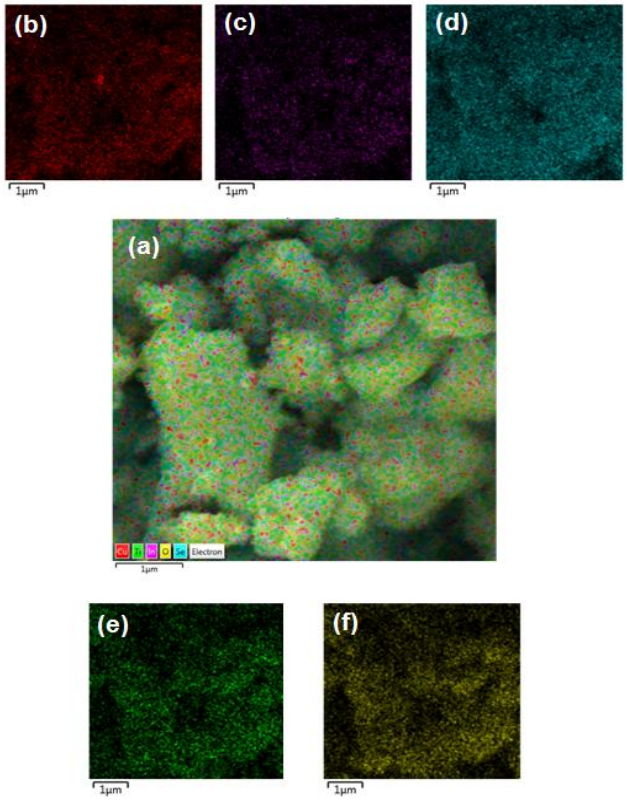

Figure 5

EDX mapping of $CuInSe_2/TiO_2$ nanocomposite. (a) EDX layered image; (b) EDX image of Cu distribution; (c) EDX image of In distribution; (d) EDX image of Se distribution; (e) EDX image of Ti distribution, and (f) EDX image of O distribution

The uniform distribution of all elements in the produced $CuInSe_2/TiO_2$ nanocomposite is well-documented utilizing the EDX mapping method. The results are shown in Figure 5. The EDX layered images of all the elements are illustrated in Figure 5a

and the individual EDX imaging for Cu, In, Se, Ti and O, respectively are shown in Figure 5b–f.

The surface composition of synthesized $CuInSe_2/TiO_2$ nanocomposite was analyzed by X-ray photoelectron spectroscopy (XPS). XPS survey and high-resolution spectra of $CuInSe_2/TiO_2$ nanocomposite are shown in Figure 6.

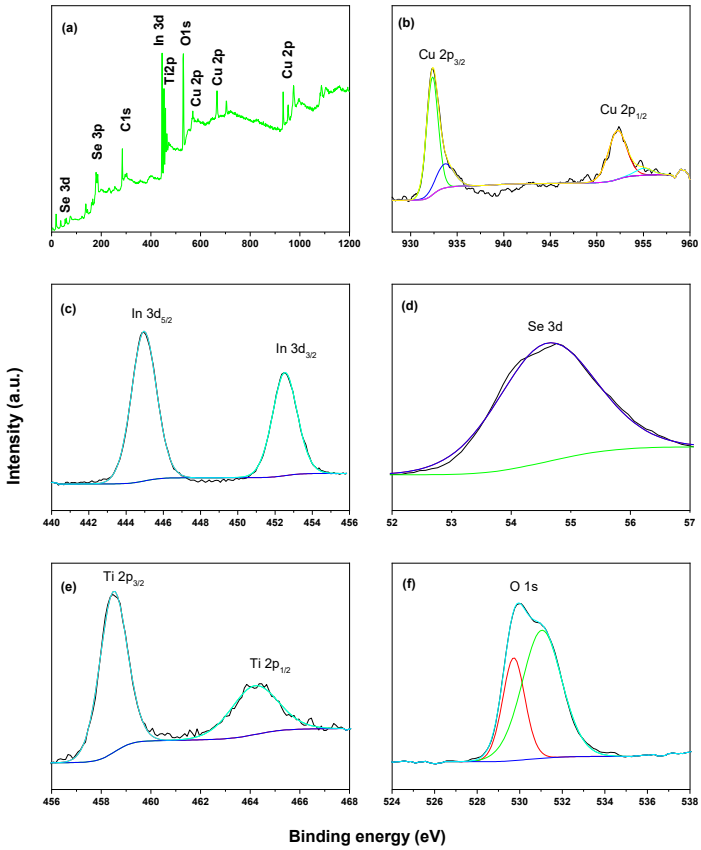

Figure 6

XPS survey spectrum (a) and high-resolution XPS spectra of $CuInSe_2/TiO_2$ nanocomposite: (b) – Cu 2p core level, (c) – In 3d core level, (d) – Se 3d core level, (e) Ti – 2p core level, (f) – O 1s core level

Cu, In, Se, Ti, O, and C as elements of interest, appear on XPS survey spectrum of the $CuInSe_2/TiO_2$ nanocomposite (Figure 6a). Regarding the high-resolution spectrum of Cu2p region (Figure 6b), there are two pairs of the spin-orbit components. Two components with higher intensity at 952.28 ($Cu2p_{1/2}$) and 932.36 eV ($Cu2p_{3/2}$), with a charge separation ΔE of 19.92 eV confirmed the monovalent nature of copper. The observed values are in accordance with the ones for $CuInSe_2$ reported in the paper (Chen et al., 2010; Kshirsagar et al., 2017). The other two components with lower intensity at 955.03 eV and 933.62 eV might be related to CuO. The doublet

components of the In3d core-level region appear at 444.96 eV ($In3d_{5/2}$) and at 452.46 eV ($In3d_{3/2}$), with a charge separation of 7.5 eV, which confirms the trivalent nature of indium (Figure 6c). As displayed in Figure 6d, the peak at 54.76 eV was indexed to $Se3d_{5/2}$, indicating the presence of Se^{2-} and proving the absence of oxide formation. $Ti2p_{3/2}$ and $Ti2p_{1/2}$ splitting components of Ti2p core-level region are found at 458.46 eV and 464.36 eV, which corresponds to the presence of TiO_2 compound. Thus, they are separated by 5.90 eV, which confirms the tetravalent nature of titanium (Figure 6e). O1s spectrum (Figure 6f) exhibits two components with binding energy positions of 529.76 eV and 531.06 eV. The results also indicate the presence of titanium dioxide. Binding energies showed that all the signals detected for individual elements Cu, In, Se, Ti and O confirmed their anticipated oxidation states. All the observed values for different elements match well with the reported ones in the paper (Kshirsagar et al., 2017).

3.3. Optical properties

The optical properties of $CuInSe_2$, TiO_2 and mechanochemically synthesized $CuInSe_2/TiO_2$ nanocomposite were investigated using UV-Vis (Figure 7) and microphotoluminescence spectroscopy at room temperature (Figure 8).

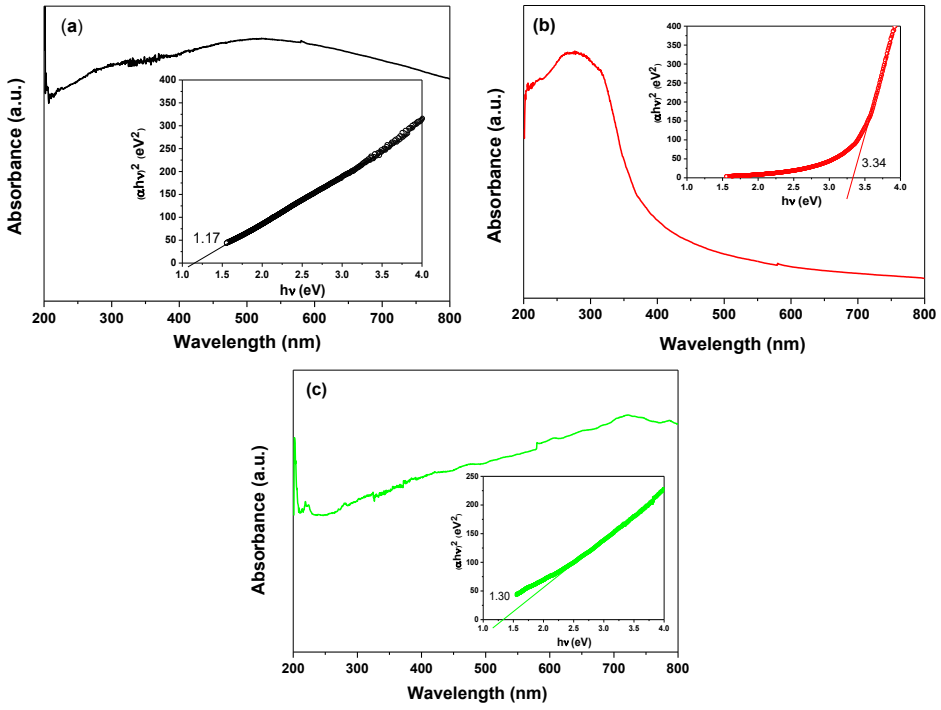

Figure 7

UV-Vis spectra and Tauc plots (inset) for $CuInSe_2$ (a), TiO_2 (b) and $CuInSe_2/TiO_2$ nanocomposite (c)

The optical band gaps were determined by plotting $(\alpha h\nu)^2$ against $(h\nu)$ and extrapolating the slope in the band edge region to zero (Equation 3) as shown in insets of Figure 7. The calculated band gap of $CuInSe_2$, TiO_2 and $CuInSe_2/TiO_2$ nanocomposite was determined to be 1.17, 3.34 and 1.30 eV, respectively. The optical band gap of TiO_2 was lightly blue-shifted in comparison with the previous reports (Kostova et al., 2015; Kostova and Dutkova, 2016). The optical band gap of $CuInSe_2$ was also blue-shifted compared to the bulk $CuInSe_2$ with band gap of 1.05 eV (Eisener et al., 1999). The observed band gap value of the nanocomposite is between those of pure $CuInSe_2$ and TiO_2 and mixing of both semiconducting materials are expected to show absorption patterns bearing the signature of both components. In comparison with pure $CuInSe_2$, the obtained $CuInSe_2/TiO_2$ nanocomposite exhibits lightly enhanced absorption in the visible light region.

Figure 8 shows the micro-photoluminescence (PL) spectrum of the mechanochemically synthesized $CuInSe_2$ and $CuInSe_2/TiO_2$ nanocomposite under laser excitation at 514 nm. In the spectrum of $CuInSe_2$ the peaks at 780 nm (1.59 eV) and 905 nm (1.37 eV) are in agreement with the peaks of nanoparticles published in the paper (Ghali et al., 2016). The interaction of $CuInSe_2$ with TiO_2 in the $CuInSe_2/TiO_2$ nanocomposite causes an increase and broadening of the emission spectrum in the 630 nm (1.96 eV) region which indicates the emission of $CuInSe_2$ nanoparticles, as described in the literature (Ghali et al., 2016). Clusters with $CuInSe_2$ quantum dots emanate a wide range of luminescence in the visible region depending upon their size and surface defects. The PL spectrum shows a gradual decrease up to the region of 1100 nm corresponding to the $CuInSe_2$ band gap (~1.12 eV).

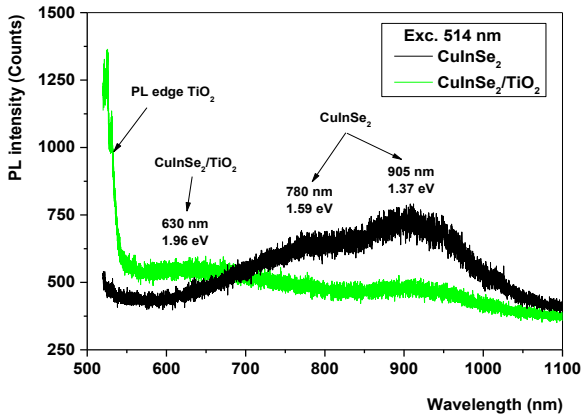

Figure 8
PL spectrum of $CuInSe_2$ and $CuInSe_2/TiO_2$ nanocomposite

3.4. Optoelectrical properties

To verify the optoelectrical properties of the mechanochemically synthesized $CuInSe_2$ and $CuInSe_2/TiO_2$ nanocomposite, the current-voltage (I-V) characteristics were measured in the dark and under illumination. The measured I-V characteristics

in the dark in Figure 9 show sufficient conductivity and are almost linear, which confirms the formation of an ohmic contact on the $CuInSe_2$ and prepared $CuInSe_2/TiO_2$ nanocomposite. After illuminating the sample, the number of generated charge carriers in the $CuInSe_2/TiO_2$ nanocomposite increases, causing an increase in the photocurrent. The results showed a photosensitivity of 5% for $CuInSe_2$ and 4.8% for $CuInSe_2/TiO_2$ at an applied voltage of 2 V compared to the current in the dark. Overall, in the nanocomposite $CuInSe_2/TiO_2$ compared to $CuInSe_2$, there was an increase in the current by 57%.

This suggests that the structure formed between $CuInSe_2$ and TiO_2 can increase the photoelectron transfer rate and promote the separation of photogenerated carriers as reported in the literature (Yu et al., 2011; Yang et al., 2022). The above-mentioned measurements of optoelectrical properties confirm the suitability of using this material for the absorber layer in solar cells.

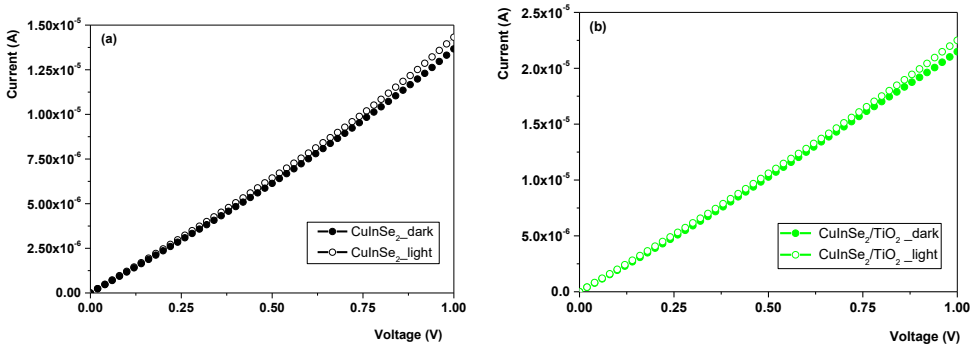

Figure 9

Current vs. Voltage (I-V) characteristics of (a) $CuInSe_2$ and (b) $CuInSe_2/TiO_2$ nanocomposite in the dark and under light illumination

4. CONCLUSIONS

In this work, $CuInSe_2/TiO_2$ nanocomposite was prepared by a simple, low-cost mechanochemical route. X-ray diffraction confirmed the nanocrystalline character of all the components of the nanocomposite, the crystallite size for $CuInSe_2$ (18 nm) being larger than in the case of both TiO_2 phases (5 and 8 nm for rutile and anatase, respectively). Raman spectroscopy confirmed the presence of both components in the nanocomposite. The morphology characterization using SEM demonstrated the homogeneity of the prepared nanocomposite. The surface properties investigated by the low-temperature nitrogen adsorption showed that the nanocrystallites are agglomerated into micron-scale particles and co-milling $CuInSe_2$ with TiO_2 led to a considerable increase of the specific surface area of the sample $CuInSe_2/TiO_2$ (13 m^2g^{-1}) in comparison with alone $CuInSe_2$. XPS analysis validated the presence of all elements in their expected oxidation states. Optical characterization indicated that the $CuInSe_2$ could extend the visible-light response range. $CuInSe_2/TiO_2$ nanocomposite exhibits strong absorption from the ultraviolet to visible region with the determined optical bandgap 1.3 eV. The current increased by 57% in $CuInSe_2/TiO_2$ nanocomposite compared to $CuInSe_2$.

This investigation has shown the possibility to prepare nanocomposite material with potential applications in optoelectronics by an environmentally friendly manner.

ACKNOWLEDGMENTS

This work was supported by the Slovak Research and Development Agency under the contracts No. APVV-18-0357, APVV-20-0437 and by the Slovak Grant Agency VEGA (project 2/0112/22 and 2/0084/23). The support of COST Action CA18112 MechSustInd (www.mechsustind.eu), supported by the COST Association (European Cooperation in Science and Technology, www.cost.eu is also acknowledged.

REFERENCES

Baláž, P., Achimovičová, M., Baláž, M., Billik, P., Cherkezova-Zheleva, Z., Criado, J. M., Delogu, F., Dutková, E., Gaffet, E., Gotor, F. J., Kumar, R., Mitov, I., Rojac, T., Senna, M., Streletskii, A. & Wieczorek-Ciurowa, K. (2013). Hallmarks of mechanochemistry: from nanoparticles to technology. *Chemical Society Reviews*, 42, pp. 7571–7637. doi: 10.1039/C3cs35468g

Baláž, P., Baláž, M., Achimovičová, M., Bujňáková, Z. & Dutková, E. (2017). Chalcogenide mechanochemistry in materials science: insight into synthesis and applications (a review). *Journal of Materials Science*, 52, pp. 11851–11890. doi:10.1007/s10853-017-1174-7

Coelho, A. A. (2018). TOPAS and TOPAS-Academic: an optimization program integrating computer algebra and crystallographic objects written in C plus. *Journal of Applied Crystallography*, 51, pp. 210–218. doi:10.1107/S1600576718000183

Das, S., Sopha, H., Krbal, M., Zazpe, R., Podzemna, V., Prikryl, J. & Macak, J. M. (2017). Electrochemical Infilling of $CuInSe_2$ within TiO_2 Nanotube Layers and Subsequent Photoelectrochemical Studies. *Chemelectrochem,* 4, pp. 495–499. doi:10.1016/j.tsf.2011.08.001

Dutkova, E., Bujnakova, L., Z., Sphotyuk, O., Jakubikova, J., Cholujova, D., Siskova, V., Daneu, N., Balaz, M., Kovac, J., Kovac, J., Briancin, J. & Demchenko, P. (2021). SDS-Stabilized $CuInSe_2$/ZnS Multinanocomposites Prepared by Mechanochemical Synthesis for Advanced Biomedical Application. *Nanomaterials*, 11. doi:Artn 6910.3390/Nano11010069

Dutkova, E., Sayagues, M. J., Kovac, J., Kovac, J., Bujnakova, Z., Briancin, J., Zorkovska, A., Balaz, P. & Ficeriova, J. (2016). Mechanochemically synthesized nanocrystalline ternary $CuInSe_2$ chalcogenide semiconductor. *Materials Letters*, 173, pp. 182–186. doi:10.1016/j.matlet.2016.03.051

Eisener, B., Wagner, M., Wolf, D. & Muller, G. (1999). Study of the intrinsic defects in solution grown $CuInSe_2$ crystals depending on the path of crystallization. *Journal of Crystal Growth*, 198, pp. 321–324. doi:10.1016/S0022-0248(98)01195-6

Evans, J. S. O. (2010). Advanced Input Files & Parametric Quantitative Analysis Using Topas. *Extending the Reach of Powder Diffraction Modelling by User Defined Macros*, 651, pp. 1–9. doi:10.4028/www.scientific.net/MSF.651.1

Ghali, M., Elnimr, M., Ali, G. F. & Yousif, B. (2016). Colloidal $CuInSe_2$ nanocrystals and thin films for low-cost photovoltaics. *Optical Materials*, 55, pp. 145–152. doi:10.1016/j.optmat.2016.03.026

Guo, Q., Kim, S. J., Kar, M., Shafarman, W. N., Birkmire, R. W., Stach, E. A., Agrawal, R. & Hillhouse, H. W. (2008). Development of $CuInSe_2$ nanocrystal and nanoring inks for low-cost solar cells. *Nano Letters*, 8, pp. 2982–2987. doi:10.1021/nl802042g

Chen, H., Yu, S. M., Shin, D. W. & Yoo, J. B. (2010). Solvothermal Synthesis and Characterization of Chalcopyrite $CuInSe_2$ Nanoparticles. *Nanoscale Research Letters*, 5, pp. 217–223. doi:10.1007/s11671-009-9468-6

Kang, F., Ao, J. P., Sun, G. Z., He, Q. & Sun, Y. (2009). Structure and photovoltaic characteristics of $CuInSe_2$ thin films prepared by pulse-reverse electrodeposition and selenization process. *Journal of Alloys and Compounds*, 478, L25–L27. doi:10.1016/j.jallcom.2008.12.020

Klenk, R., Klaer, J., Koble, C., Mainz, R., Merdes, S., Rodriguez-Alvarez, H., Scheer, R. & Schock, H. W. (2011). Development of $CuInS_2$-based solar cells and modules. *Solar Energy Materials and Solar Cells*, 95, pp. 1441–1445. doi:10.1016/j.solmat.2010.11.001

Kostova, N. & Dutkova, E. (2016). Mechanochemical synthesis and properties of ZnS/TiO_2 composites. *Bulgarian Chemical Communications*, 48, pp. 161–166.

Kostova, N. G., Dutkova, E., Eliyas, A., Stoyanova-Eliyas, E., Fabian, M. & Balaz, P. (2015). Mechanochemical synthesis, characterization, and photocatalytic activity of CdS/TiO_2 composites in air purification. *Bulgarian Chemical Communications*, 47, pp. 87–93.

Kshirsagar, A. S., Gautam, A. & Khanna, P. K. (2017). Efficient photo-catalytic oxidative degradation of organic dyes using $CuInSe_2/TiO_2$ hybrid hetero-nanostructures. *Journal of Photochemistry and Photobiology a-Chemistry*, 349, pp. 73–90. doi:10.1016/j.jphotochem.2017.08.058

Liao, Y. L., Zhang, H. W., Zhong, Z. Y., Jia, L. J., Bai, F. M., Li, J., Zhong, P., Chen, H. & Zhang, J. (2013). Enhanced Visible-Photocatalytic Activity of Anodic TiO_2 Nanotubes Film via Decoration with $CuInSe_2$ Nanocrystals. *ACS Applied Materials & Interfaces*, 5, pp. 11022–11028. doi:10.1021/am403264q

Rincon, C. & Ramirez, F. J. (1992). Lattice-Vibrations of $CuInSe_2$ and $CuGaSe_2$ by Raman Microspectrometry. *Journal of Applied Physics*, 72, pp. 4321–4324.

Tuschel, D. (2019). Molecular Spectroscopy Workbench Raman Spectroscopy and Polymorphism. *Spectroscopy*, 34, pp. 10–21.

Valdes, M., Goossens, A. & Vazquez, M. (2011). Sulfurization of electrodeposited $CuInSe_2$-based solar cells. *Materials Chemistry and Physics*, 125, pp. 860–865. doi:10.1016/j.matchemphys.2010.09.032

Wang, Q. Y., Qiao, J. L., Zhou, J. & Gao, S. M. (2015). Fabrication of $CuInSe_2$ quantum dots sensitized TiO_2 nanotube arrays for enhancing visible light photoelectrochemical performance. *Electrochimica Acta*, 167, pp. 470–475. doi:10.1016/j.electacta.2014.08.037

Wu, Z. M., Tong, X., Sheng, P. T., Li, W. L., Yin, X. H., Zou, J. M. & Cai, Q. Y. (2015). Fabrication of high-performance $CuInSe_2$ nanocrystals-modified TiO_2 NTs for photocatalytic degradation applications. *Applied Surface Science*, 351, pp. 309–315. doi:10.1016/j.apsusc.2015.05.147

Yang, Z. Y., Li, H., Cui, X. Q., Zhu, J. K., Li, Y. H., Zhang, P. F. & Li, J. R. (2022). Highly Efficient $CuInSe_2$ Sensitized TiO_2 Nanotube Films for Photocathodic Protection of 316 Stainless Steel. *Coatings*, 12. doi:Artn 1448 10.3390/Coatings12101448

Yu, Y. Y., Chien, W. C., Ko, Y. H. & Chen, S. H. (2011). Preparation and characterization of P_3HT:$CuInSe_2$:TiO_2 thin film for hybrid solar cell applications. *Thin Solid Films*, 520, pp. 1503–1510. doi:10.1016/j.tsf.2011.08.001

Zaretskaya, E. P., Gremenok, V. F., Riede, V., Schmitz, W., Bente, K., Zalesski, V. B. & Ermakov, O. (2003). Raman spectroscopy of $CuInSe_2$ thin films prepared by selenization. *Journal of Physics and Chemistry of Solids*, 64, pp. 1989–1993. doi:10.1016/S0022-3697(03)00216-6

Zhang, Y. N., Yang, Y., Hou, Z. Y., Jiang, X. J., Zhang, L., Yang, Y. Y. & Wang, Y. L. (2020). The effect of reaction temperature and time on $CuInSe_2$ quantum dots by solvothermal method. *AIP Advances*, 10. doi:Artn03531310.1063/1.5135065